ADVANCES IN ATMOSPHERIC SCIENCES, VOL. 35, DECEMBER 2018, 1491–1504

• **Original Paper** •

Estimating the Predictability Limit of Tropical Cyclone Tracks over the Western North Pacific Using Observational Data

Quanjia ZHONG[1,2,3], Lifeng ZHANG[2], Jianping LI[4,5], Ruiqiang DING[*1,4], and Jie FENG[6]

[1]*State Key Laboratory of Numerical Modeling for Atmospheric Sciences and Geophysical Fluid Dynamics, Institute of Atmospheric Physics, Chinese Academy of Sciences, Beijing* 100029*, China*

[2]*College of Meteorology and Oceanography, National University of Defense Technology, Nanjing* 211101*, China*

[3]*College of Earth Science, University of Chinese Academy of Sciences, Beijing* 100049*, China*

[4]*Laboratory for Regional Oceanography and Numerical Modeling, Qingdao National Laboratory for Marine Science and Technology, Qingdao* 266237*, China*

[5]*College of Global Change and Earth System Sciences, Beijing Normal University, Beijing* 100875*, China*

[6]*School of Meteorology, University of Oklahoma, Norman OK* 73072*, USA*

(Received 10 January 2018; revised 9 June 2018; accepted 4 July 2018)

ABSTRACT

In this study, the nonlinear local Lyapunov exponent (NLLE) approach was used to quantitatively determine the predictability limit of tropical cyclone (TC) tracks based on observed TC track data obtained from the Joint Typhoon Warning Center. The results show that the predictability limit of all TC tracks over the whole western North Pacific (WNP) basin is about 102 h, and the average lifetime of all TC tracks is about 174 h. The predictability limits of the TC tracks for short-, medium-, and long-lived TCs are approximately 72 h, 120 h, and 132 h, respectively. The predictability limit of the TC tracks depends on the TC genesis location, lifetime, and intensity, and further analysis indicated that these three metrics are closely related. The more intense and longer-lived TCs tend to be generated on the eastern side of the WNP (EWNP), whereas the weaker and shorter-lived TCs tend to form in the west of the WNP (WWNP) and the South China Sea (SCS). The relatively stronger and longer-lived TCs, which are generated mainly in the EWNP, have a longer travel time before they curve northeastwards and hence tend to be more predictable than the relatively weaker and shorter-lived TCs that form in the WWNP region and SCS. Furthermore, the results show that the predictability limit of the TC tracks obtained from the best-track data may be underestimated due to the relatively short observational records currently available. Further work is needed, employing a numerical model to assess the predictability of TC tracks.

Key words: predictability, tropical cyclone tracks, nonlinear local Lyapunov exponent

Citation: Zhong, Q. J., L. F. Zhang, J. P. Li, R. Q. Ding, and J. Feng, 2018: Estimating the predictability limit of tropical cyclone tracks over the western North Pacific using observational data. *Adv. Atmos. Sci.*, **35**(12), 1491–1504, https://doi.org/10.1007/s00376-018-8008-7.

1. Introduction

Tropical cyclones (TCs) are destructive weather phenomena that pose a great threat to life and property, and are the cause of many natural disasters. Accordingly, more accurate forecasts of TC tracks would help to reduce the loss of life and minimize the damage associated with TCs. With the development of numerical models and the more effective use of observational data, great improvements in the accuracy with which TC tracks can be forecast have been made in recent decades (Sampson et al., 2006; Goerss, 2009; Elsberry, 2014; Qi et al., 2014; Thanh et al., 2016). However, as a mesoscale weather system, the predictability of TC tracks is limited by the chaotic nature of the system itself (Thompson, 1957; Lorenz, 1963, 1969). The TC track, as one of the most significant forecast parameters, can be further improved with better understanding of the associated predictability limit (Zhang and Krishnamurti, 1997; Elsberry, 2007; Elsberry et al., 2010; Li et al., 2016). Therefore, the estimation of the predictability limits of TC tracks is worthy of further investigation.

Numerous studies have investigated the predictability of TC tracks in different basins (Chan and Gray, 1982; Fraedrich and Leslie, 1989; Bender et al., 1993; Goerss, 2000; Elsberry et al., 2010; Aiyyer, 2015; Peng et al., 2015; Munsell, 2016). Since the early 1980s, a nonlinear systems analysis approach known as the correlation integral has been used to examine the dimensionality of the attractor in a dynamical system and the growth rate of the initial small error, which is

* Corresponding author: Ruiqiang DING
Email: drq@mail.iap.ac.cn

a relevant measure of the predictability of a dynamical system (Grassberger and Procaccia, 1984; Nicolis and Nicolis, 1984; Fraedrich, 1987; Leslie et al., 1998). Based on best-track data, Fraedrich and Leslie (1989) used the correlation integral method to measure the error growth of initially close sections of TC tracks, and then estimated the predictability of these tracks. Their results showed that the *e*-folding growth timescale of the TC track error is approximately 24 h (1 day) in the Australian Basin. Using a similar approach, Aberson (1998) and Aberson and Sampson (2003) calculated the *e*-folding growth timescale of TC track error in other basins, and revealed that the predictability timescale of TC tracks is roughly 60 h in the Northwest Pacific, 42 h in the Northeast Pacific, and nearly 60 h in the Atlantic Basin. These results suggest that the predictability of TC tracks varies between basins and that TC tracks in the Australian Basin are likely to be the least predictable. In addition to the nonlinear systems analysis approach, several studies have examined the predictability of TC tracks using numerical models (Leslie et al., 1998; Fiorino, 2009; Plu, 2011; Qin et al., 2013; Munsell and Zhang, 2014; Poterjoy and Zhang, 2014). For example, based on several up-to-date numerical models, including the global model of the European Centre for Medium-Range Weather Forecasts, Plu (2011) suggested that the doubling time of small initial error is between 30 and 50 h.

These previous studies have significantly improved our understanding of TC track predictability. However, they estimated the predictability of the TC tracks using mainly the error *e*-folding growth time or the error doubling time. Some studies have pointed out that these commonly used parameters might not be a good measure of predictability, mainly because they are usually determined by extrapolation from the small error and are extremely sensitive to the method of extrapolation (Heckley, 1985; Dalcher and Kalnay, 1987). Arpe and Klinker (1986) also argued that it is difficult to measure the doubling time of small initial error directly. Moreover, the error *e*-folding growth time and the error doubling time have another limitation in that they are defined by assuming that the error is sufficiently small that their evolution can be governed approximately by the linearized error growth equations (Lacarra and Talagrand, 1988; Mu, 2000). Given the limitations of the error e-folding growth time or the error doubling time in measuring the predictability of TC tracks, in this paper we present a new method, based on nonlinear error growth dynamics, that helps to quantitatively estimate the predictability limit of TC tracks.

Over the last decade, a new approach, based on the nonlinear local Lyapunov exponent (NLLE), has been introduced into the study of atmospheric and oceanic predictability (Chen et al., 2006; Ding and Li, 2007). This NLLE approach is superior to the traditional Lyapunov exponent, which is based on linear error dynamics, for quantitatively estimating the predictability limit of atmospheric and oceanic variables because it can be applied to predictability investigations of finite-size initial error and the error average growth at a finite time. With the NLLE and its derivatives, the predictability limit can be efficiently and quantitatively determined. Li and Ding (2011) developed a reasonable and efficient algorithm that is based on local dynamical analogs (LDAs) to calculate the NLLE and its derivatives using observational data for the investigation of atmospheric and oceanic predictability. Much recent research has applied the NLLE approach to the study of atmospheric predictability based on observational data and obtained the spatiotemporal characteristics of the predictability limit of different atmospheric variables, including the geopotential height, temperature, and precipitation (Ding and Li, 2009b; Ding et al., 2010; Li and Ding, 2013; Li et al., 2014; Liu et al., 2016).

The remainder of this paper is arranged as follows. In section 2, the observed TC data (best-track data) used in this investigation are briefly described and the NLLE method and its application based on observational data are introduced. Section 3 presents the predictability limit of the TC tracks over the whole western North Pacific (WNP) basin. Section 4 shows the dependence of TC track predictability on TC genesis location, lifetime, and intensity. The linkages among the predictability limit of the TC tracks, the TC genesis location, lifetime, and intensity are discussed in section 5. Finally, a summary of our major findings is provided in section 6.

2. Data and methods

2.1. *Observational data*

We use the best-track data for the period 1945–2013 provided by the Joint Typhoon Warning Center (JTWC), downloaded from http://www.usno.navy.mil/NOOC/nmfc-ph/RSS/jtwc/best_tracks/, to investigate TC track predictability over the whole WNP basin. The WNP basin, including the SCS, covers the area bounded by (0°–30°N, 100°–180°E). The TC dataset contains the maximum wind speed, central surface pressure, and observations of the central positions (latitude and longitude) for each 6-h interval. There were 1814 TCs with lifetimes that exceeded 48 h across the whole WNP between 1945 and 2013 (Fig. 1a). In addition to the best-track data from the JTWC, the most recent version of the international best-track archive for climate stewardship (IBTrACS v03r06) database, which is a new global TC best-track dataset, is used to verify the results generated using the JTWC data (Knapp et al., 2010). The IBTrACS dataset provides the first publicly available centralized repository of global TC best-track data from the JTWC, Japan Meteorological Agency, China Meteorological Administration, and other agencies. As numerous TCs were reported by other agencies in the WNP basin, some TCs obtained from the IBTrACS dataset may not be included in the best-track data from the JTWC.

2.2. *The NLLE approach*

For vector $\boldsymbol{x}(t_0)$ at time t_0, the NLLE, λ, is defined as follows:

$$\lambda(\boldsymbol{x}(t_0), \boldsymbol{\delta}(t_0), \tau) = \frac{1}{\tau} \ln \frac{\|\boldsymbol{\delta}(t_0 + \tau)\|}{\|\boldsymbol{\delta}(t_0)\|} , \qquad (1)$$

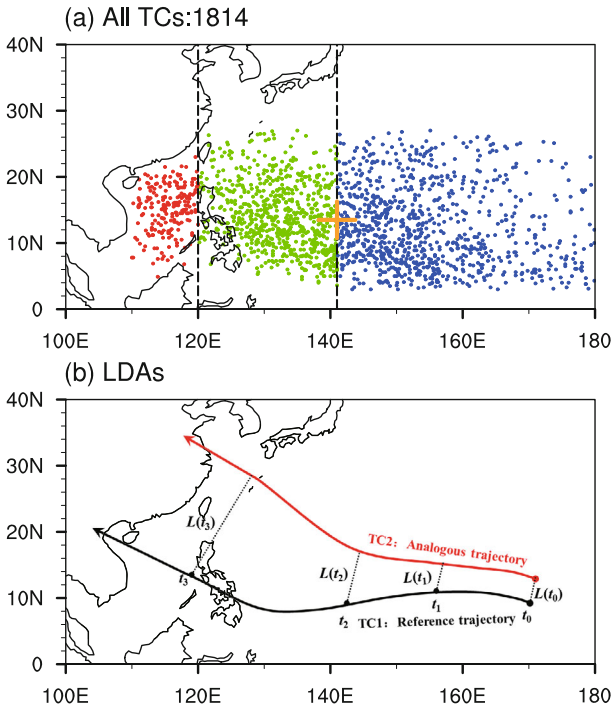

Fig. 1. (a) Spatial distribution of genesis locations of all TCs over the whole WNP basin. The dots denote the genesis locations of TCs generated in the SCS (red dots), WWNP (green dots), and EWNP (blue dots), and the cross denotes the MGL of all TCs over the whole WNP basin. The longitudinal boundaries of these three subregions are at 110°E, 120°E, 141°E, and 180°. (b) Schematic representation of the evolution procedure used to calculate the NLLE from the best-track data. The evolution trajectory of an analog of the reference TC at time t_i $(i = 0, 1, 2, \ldots)$ is denoted as an analogous trajectory. The growth rate of the absolute distance between the reference trajectory and its analogous trajectory is used to estimate the NLLE.

where $\lambda(\boldsymbol{x}(t_0), \boldsymbol{\delta}(t_0), \tau)$ depends on the initial state $\boldsymbol{x}(t_0)$ of the reference orbit in phase space, the initial error $\boldsymbol{\delta}(t_0)$, and the evolution time τ (Chen et al., 2006; Ding et al., 2007; Ding and Li, 2007). The NLLE differs from the traditional Lyapunov exponent, which is determined solely from the initial state $\boldsymbol{x}(t_0)$ and the evolution time step τ, rather than from the initial error $\boldsymbol{\delta}(t_0)$ (Yoden and Nomura, 1993; Kazantsev, 1999; Ziehmann et al., 2000). Moreover, the NLLE measures the average growth rate of the initial error based on the nonlinear error growth equations, thereby overcoming the limitations of the traditional Lyapunov exponent, which uses the linearized error growth equation. Figure 2 is a schematic illustration of the mean error growth measured in terms of the sufficiently small differences between the two initial states for a dynamical system, as obtained using the linear Lyapunov and NLLE methods. For short time intervals, the error shows rapid linear growth. Over time, the evolution of the error begins to depart from a linear trend, indicating that the evolution of the error enters a nonlinear growth phase with a gradually decreasing growth rate, and finally reaches saturation level. In contrast, the evolution of the error obtained from the linear Lyapunov method shows continuous linear growth (Fig. 2). Therefore, compared with the traditional Lyapunov exponent, the NLLE approach is more applicable to describing the processes associated with the nonlinear error growth of dynamical systems and more suitable for describing the growth of infinitesimal or finite-size initial error (Ding and Li, 2012; Ding et al., 2016)

The ensemble mean NLLE over the global attractor of the dynamical system is given by

$$\bar{\lambda}(\boldsymbol{\delta}(t_0), \tau) = \langle \lambda(\boldsymbol{x}(t_0), \boldsymbol{\delta}(t_0), \tau) \rangle_N, \quad (N \to \infty) , \qquad (2)$$

where $\langle\ \rangle_N$ denotes the ensemble average of samples of sufficiently large size N $(N \to \infty)$. The ensemble-mean NLLE reflects the global evolution of mean error growth over an attractor and can measure the global-mean predictability.

Based on the mean NLLE, the mean relative growth of the initial error (RGIE), which is defined as the ratio of the error at the evolution time τ to the initial error, can be obtained as follows:

$$\bar{\Phi}(\boldsymbol{\delta}(t_0), \tau) = \exp[\bar{\lambda}(\boldsymbol{\delta}(t_0), \tau)\tau] \xrightarrow{\mathrm{P}} c(N \to \infty) , \qquad (3)$$

where $\xrightarrow{\mathrm{P}}$ denotes the convergence in probability and $\bar{\lambda}(\delta(t_0), \tau)$ is the ensemble mean NLLE of the dynamic system. Using the theorem from Ding and Li (2007), the constant c can be considered as the theoretical saturation level of the RGIE, when the sample size N tends towards infinity. Once the mean error growth reaches saturation level, almost all information on the initial state is lost and the prediction becomes meaningless. Therefore, the predictability limit can be quantitatively determined based on the theoretical saturation value (Ding and Li, 2007). As a measure of predictability, the predictability limit is superior to the error e-folding growth time or the error doubling time and, as such, information on the predictability limit can be used as a basic guideline for improving prediction models.

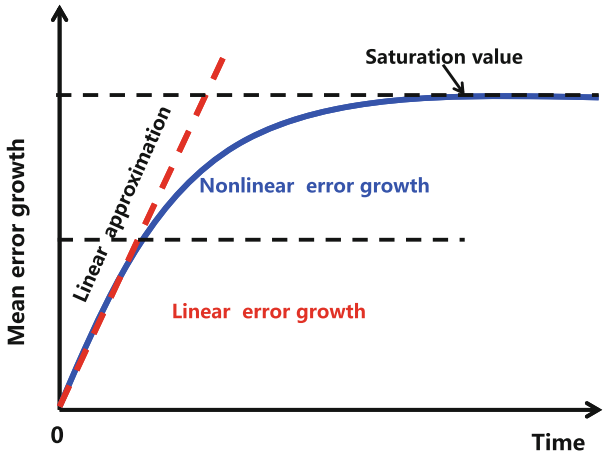

Fig. 2. Schematic illustration of the mean error growth of a dynamical system, as obtained using the NLLE method. The mean error growth (y-axis) uses a logarithmic scale to amplify the differences between the linear and nonlinear error evolutions.

2.3. *Estimation of the NLLE from observational data*

The NLLE approach has been widely used to study the predictability of weather and climate (Ding et al., 2010; Li and Ding, 2011; Shi and Ding, 2012; Liu et al., 2016). In comparison with the linear approach, one major advantage of the NLLE approach is that the NLLE and its derivatives can be used to quantitatively determine the limit of weather and climate predictability. In addition, the NLLE approach can be used to determine the spatial distribution of the limit of weather and climate predictability by making use of observational data. By developing an algorithm based on LDAs, the mean NLLE and its derivatives can be calculated using observational data. The general purpose of the algorithm is to find the analogs of the pattern of evolution in the observational time series.

In this study, based on best-track data, the predictability of TC tracks is measured in terms of the mean error growth of TC tracks, which is computed from the divergence of the evolutionary tracks of two initially analogous TCs. The determination of two analogous TCs is based on the initial distance, which is the distance between the genesis locations (along a great circle) of two TCs, and the evolutionary distance, which is the mean distance between two TCs evolving over an early time interval after the TCs formed. The two independent TCs have a sufficiently small initial distance, which ensures that their genesis locations are close, and the small evolutionary distance ensures the similarity of their directions of motion. To ensure similarity of the large-scale environmental steering flows for the two TCs, we search for an analog of the reference TC from all TCs that formed in a similar "season" but in different years (i.e., ±45 days of the genesis time of the reference TC). Note that the genesis time and location are defined as the time and location, respectively, of the first record of a TC track. Furthermore, we consider the similarity of initial intensity (the present intensity at the genesis time) when two analogous TCs are chosen. The conditions outlined above help us to find truly analogous TCs and to exclude, as much as possible, non-analogous TCs (Fig. 1b). A detailed description of the algorithm used to find the analogous TCs and to estimate the NLLE based on the best-track data is given in Appendices A and B.

3. Mean predictability limit of all TC tracks

In this study, the initial error is the distance (along a great circle) between the genesis locations of two analogous TCs, and the real-time track error is the distance (along a great circle) between the real-time locations of the two analogous TCs. The mean error growth represents the RGIE, which is defined as the ratio of the real-time track error at the time of evolution to the initial error. Based on the NLLE approach, the mean error growth of TC tracks over time can be obtained using the JTWC and IBTrACS datasets. Figure 3a shows the mean error growth of the TC tracks over the whole WNP basin, based on the JTWC best-track data. For a short time interval, the mean error of the TC tracks shows rapid linear growth. With increasing time, the evolution of the mean error enters a nonlinear growth phase, and this is characterized by a relatively slow increase that finally reaches saturation level. The mean error associated with the TC tracks eventually reaches a saturation point that reflects a total loss of information regarding the initial state, meaning that the track prediction becomes meaningless. Here, to reduce the effects of sampling fluctuations, we define the predictability limit as the time at which the mean error reaches 95% of its saturation level (Ding and Li, 2009a; Li and Ding, 2013; Ding et al., 2016). It should be noted that the time at which error growth reaches saturation depends mainly on the dynamical characteristics of the system, and thus is a relatively objective criterion with which to quantitatively determine the predictability limit. From Fig. 3a, the mean predictability limit of the TC tracks based on the JTWC best-track data is approximately 102 h (4.25 days) over the whole WNP basin. This is in agreement with the results shown in Fig. 3b, in which the mean error and the predictability limit of the TC tracks were obtained from the IBTrACS database using the NLLE method. Hereafter, having considered the consistency of the predictability limit of the TC tracks obtained from the JTWC and IBTrACS datasets, we use mainly the JTWC best-track

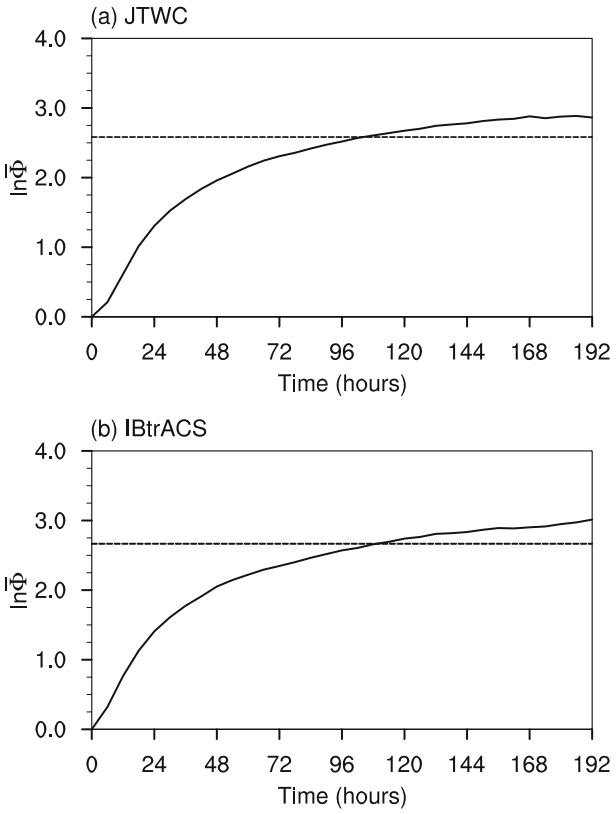

Fig. 3. Mean error growth of all TC tracks over the whole WNP basin, obtained from the (a) JTWC and (b) IBTrACS best-track data. Note that the mean error growth on the *y*-axis uses a logarithmic scale to amplify the differences between linear and nonlinear error evolutions. The dashed line represents the 95% level of the saturation value obtained by taking the average of the mean error growth after 168 h.

data to examine the error growth and predictability limit of the TC tracks.

According to the above analysis, although the predictability limit of the TC tracks exceeds 100 h for both datasets, the relatively short observational records that are currently available make it likely that the predictability limit of the TC tracks is underestimated based on the best-track data. The total number of TCs that develop across the whole WNP basin is relatively small. Some false analogs were inevitably found in the best-track data, and these caused the initial error associated with the TC tracks to increase (because analogous TCs would be more difficult to find). This may accelerate the growth of the mean error and reduce the estimate of the predictability limit. Considering the underestimation of the predictability limit of the TC tracks based on the observational data, there is considerable potential for improving the forecast skill of TC tracks. As pointed out by Plu (2011), the predictability limit would provide objective information that would allow us to determine the improvement that could be expected from future advances in data assimilation and numerical models.

In previous studies, evaluations of the forecast track error associated with numerical models of TC tracks were performed using along- and cross-track components (Elsberry and Peak, 1986; Goerss, 2000; Sampson et al., 2006). Here, the magnitudes of the track error between analogous TCs are also defined in terms of the cross- and along-track components to examine the predictability of TC tracks based on the NLLE method. We use the convention that the along- and cross-track error represent the speed bias (fast or slow) and direction bias (right or left), respectively, of the reference TC, relative to the verified position of the analogous TC. Figure 4 shows the mean error growth of the along- and cross-track components of the TC tracks. There are only trivial differences between the error growth curves of the two components over a short time interval. Afterwards, however, the mean error of the along-track component increases more rapidly than that of the cross-track component. This result indicates that the error of the along-track component dominates the error growth of all TC tracks.

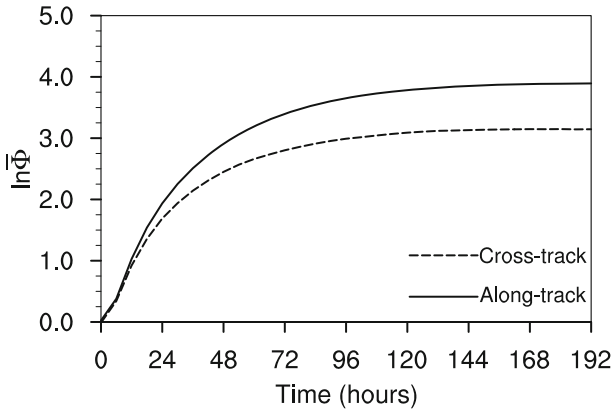

Fig. 4. As in Fig. 3 but for the mean error growth of the along- and cross-track components of the TC tracks.

4. Dependence of the predictability of TC tracks on the genesis location, lifetime, and intensity

The above results focus primarily on the predictability limit of all TC tracks over the whole WNP basin. However, the response of the predictability limit of TC tracks to changes in genesis location, lifetime, and intensity remains unclear. Consequently, in this section, we explore the dependence of the predictability of TC tracks on these factors.

4.1. *TC genesis location*

TC tracks vary in space and TCs are generated over a broad area across the entire WNP basin. The spatial distribution of TC track predictability can be approximated by functions depending on the genesis locations of the TCs. To determine the spatial distribution of TC track predictability, we first quantitatively estimated the predictability limit of the individual TC tracks using the NLLE method and the latitude and longitude of the TC genesis locations. This estimation of the predictability limit was then interpolated onto a 2° latitude by 2° longitude spatial grid across the WNP basin. Figure 5a shows the spatial distribution of the predictability limit of the TC tracks over the WNP basin. The predictability limit of the TC tracks ranges from 48 to 120 h (2–5 days) over the basin, and depends largely on TC genesis location. Overall, the predictability limit of the TC tracks shows a gradual increase from 100°E to 180°, and this is highlighted by the meridional mean (Fig. 5b). The predictability limit of the TC tracks is lowest (<72 h) in the SCS (110°–120°E), possibly because the TCs generated in this region are already closer to the mainland or islands (such as the Philippines), and so TC motion is complicated by the influence of topography and boundary layer friction (Chan, 2005; Wong and Chan, 2006). In the western region of the WNP (120°–140°E), the predictability limit of the TC tracks is relatively high, ranging from 72 to 96 h (3–4 days). In the eastern region of the WNP (140°E–180°, and especially the southeastern region of the WNP), the predictability limit of the TC tracks is greater than those in the SCS and the western region of the WNP. We speculate that the future TC tracks may be affected by the genesis locations. When the TCs are generated over the central and eastern regions of the WNP, their initial movement is typically to the west or northwest at a relatively steady rate, but this is followed by an eventual poleward turn. Such turning is referred to as recurvature, and these TC tracks tend to have relatively low predictability. This may explain why the predictability limit of the TC tracks depends strongly on TC prevailing tracks and genesis locations. Therefore, we must compare the predictability limit of the TC tracks originating from different regions of the WNP basin.

The genesis location for each TC is considered to be a point (see Fig. 1a). The mean genesis location (MGL) for all TCs formed in the WNP basin is (13.5°N, 141°E) (orange cross in Fig. 1a). Based on the longitude of the MGL, we divided the WNP (120°E–180°) into two subregions: the east

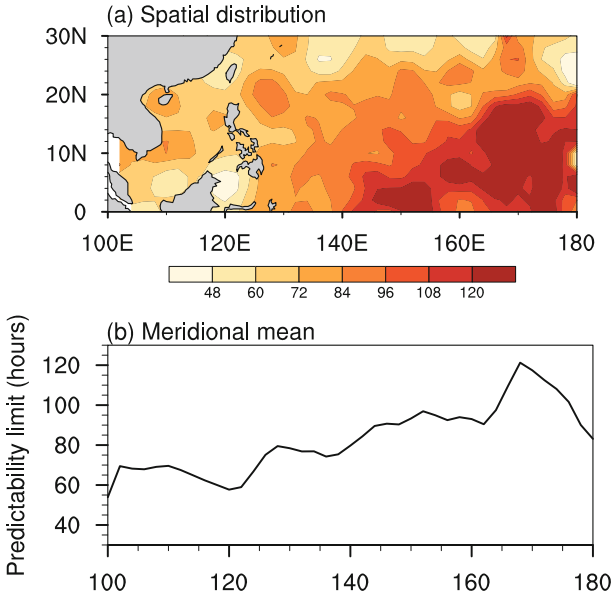

Fig. 5. (a) Spatial distribution of the predictability limit of the individual TC track obtained from the JTWC best track data and (b) its meridional mean profile.

WNP (EWNP; east of 141°E) and the west WNP (WWNP; west of 141°E). In addition to these two subregions, we treated the SCS as a separate region because TCs generated here behave differently, and this is a statistical characteristic of genesis number and the mean lifetime of these TCs when compared with those from the WNP (Wang et al., 2007; Yan et al., 2012). Over the study period (1945–2013), the numbers of TCs observed in the SCS, WWNP, and EWNP were 209, 712, and 893, respectively.

We next examined the mean error growth of the TC tracks in the SCS, WWNP, and EWNP regions and found that the mean error of the TC tracks in the SCS was the first to reach saturation state, followed by the WWNP, and then the EWNP (Fig. 6). We used these error growth curves from the TC tracks in these regions to determine that the predictability limits of the TC tracks in the SCS, WWNP, and EWNP regions were about 60 h (2.5 days), 84 h (3.5 days), and 108 h (4.5 days), respectively. This indicates that the predictability limit of the TC tracks in the EWNP is much higher than that in the SCS, and the predictability limit of the TC tracks gradually increases from the SCS to EWNP, which is consistent with the results shown in Fig. 5a.

4.2. *TC lifetime*

The above results indicate that the predictability limit of the TC tracks shows considerable dependence on TC genesis location over the whole WNP basin. Previous studies have found that TCs generated in different regions have differing lifetimes (Wang and Chan, 2002; Camargo and Sobel, 2005; Camargo et al., 2007; Murakami et al., 2011). Therefore, it is important to consider whether there is any connection between the lifetime and predictability limit of TC tracks. To address this question, we classified all TCs into

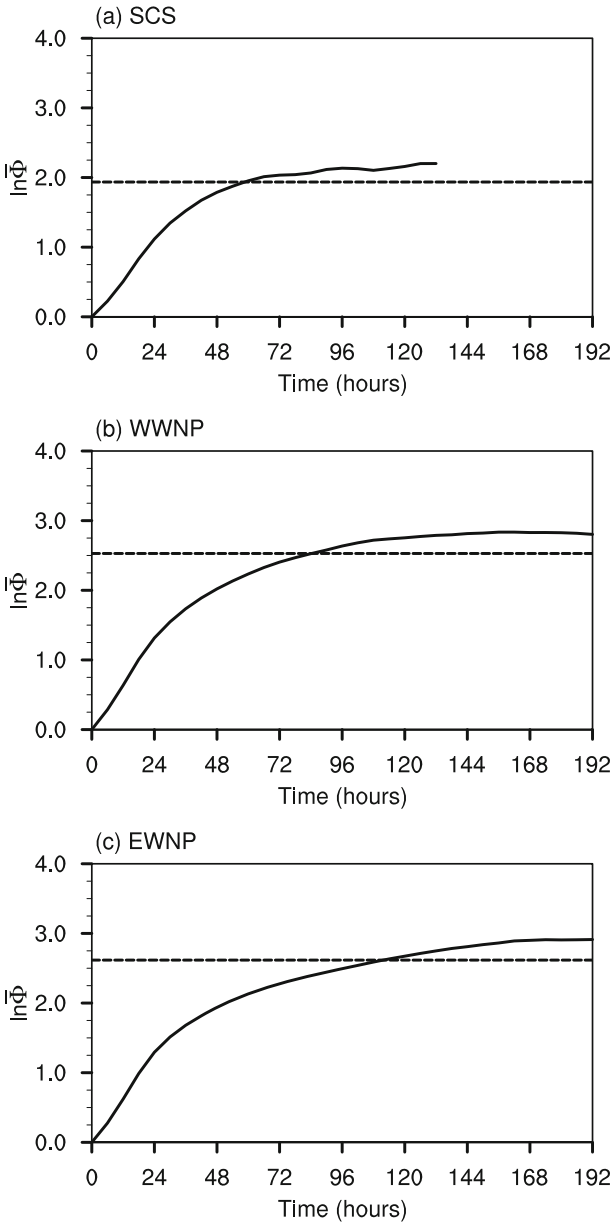

Fig. 6. As in Fig. 2 but for the mean error growth of the TC tracks in the (a) SCS, (b) WWNP, and (c) EWNP.

three groups according to their lifetime: short-lived (lifetime <144 h), medium-lived (lifetime 144–216 h), and long-lived (lifetime >216 h). The number of TCs in each group was 689, 602, and 523, respectively. This classification scheme is broadly similar to that used by Camargo and Sobel (2005), but they classified TCs into only two groups; i.e., short-lived and long-lived.

Figure 7 shows that the mean error associated with the TC tracks of short-, medium-, and long-lived TCs gradually depart from each other after about 12 h. The mean error of the medium- and long-lived TC tracks show relatively slow growth, and ultimately reach saturation state after a few days (about 168 h). By comparison, the mean error growth of the short-lived TC tracks increases at the fastest rate of these

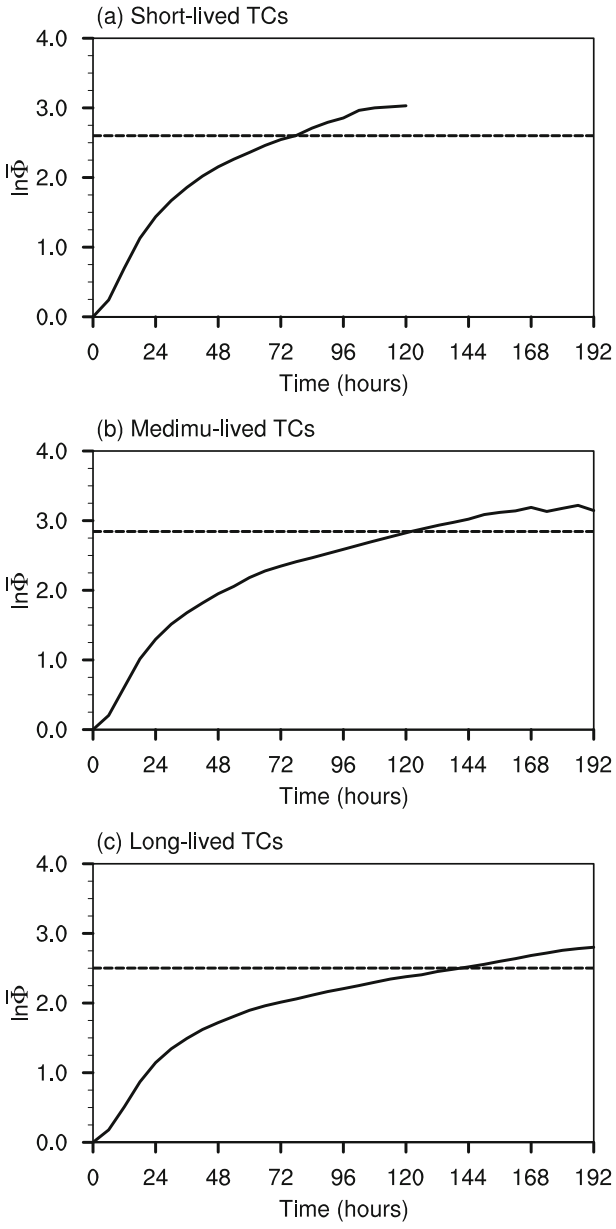

Fig. 7. As in Fig. 2 but for the mean error growth of (a) short-lived, (b) medium-lived, and (c) long-lived TC tracks.

three groups. As the quick decay of the short-lived TCs results in a relatively short lifetime and restricted dataset, error saturation values for the short-lived TC tracks do not exist after 120 h. Considering that the mean error of short-lived TC tracks shows extremely slow growth at the end (close to the saturation state), the maximal error value of the short-lived TC tracks was taken as the approximate saturation value, making it suitable for estimating the predictability limit of the TC tracks. It should be noted that this might lead to a slight underestimation of the predictability limit of short-lived TC tracks. According to the 95% error saturation criterion, the predictability limit of the short-, medium-, and long-lived TC tracks was approximately 72 h (3 days), 120 h (5 days), and 132 h (5.5 days), respectively. We found that the predictability limit of the long-lived TC tracks was about twice that of the short-lived TC tracks. These results indicate that the predictability limit of TC tracks is generally associated with changes in TC lifetime, and a TC with a relatively long lifetime may be favorable for a relatively high predictability of TC track.

4.3. *TC intensity*

According to recent studies of TC activity, intensity is one of the most important TC metrics (Knutson et al., 2010; Walsh et al., 2016). To further clarify the effect of TC intensity on the predictability limit of TC tracks, we classified TC intensity into four levels based on the maximum sustained wind speed: tropical depression (TD; 10.8–17.1 m s^{-1}); tropical storm (TS; 17.2–32.6 m s^{-1}, including tropical storm and severe tropical storm); typhoon (TY; 32.7–41.4 m s^{-1}); and severe typhoon (STY; >41.5 m s^{-1}, including severe typhoon and super typhoon), which is similar to the classification scheme used in previous studies (Wu et al., 2012; Zhang et al., 2012). As intensity changes throughout the lifetime of a TC, the intensity levels in this investigation were based on the peak intensity over the lifetime. The mean error growth of the TC tracks in the four intensity categories (TD, TS, TY, and STY) is shown in Fig. 8. The STY track has the highest predictability limit of the four categories, at approximately 114 h (4.75 days), and is significantly higher than that of the TD tracks (about 60 h). In contrast to the TD tracks, the predictability limits of the TS and TY tracks are also relatively high, with values of 96 h (4 days) and 102 h (4.25 days), respectively. These results suggest that the predictability limit of the TC tracks differs for different TC intensities, and that relatively weak (strong) TCs tend to have a relatively low (high) TC track predictability.

5. Discussion

5.1. *Distribution of genesis location for different TC types*

In section 4, we demonstrated that the predictability limit of TC tracks depends on the genesis location, lifetime, and intensity of the TCs. Next, we show that the lifetime, intensity, and genesis location are closely related. Figures 9a–c show the spatial distributions of the genesis locations of the short-, medium-, and long-lived TCs, respectively, over the whole WNP basin. The whole WNP domain is also divided into three subregions: the SCS, WWNP, and EWNP. The most striking feature of the spatial distributions is the prominent west–east shift in the genesis location between the short-lived and long-lived TCs. More short-lived TCs were generated to the west of 141°E (including the SCS and WWNP regions), whereas most of the long-lived TCs were generated to the east of 141°E (i.e., the EWNP region). In contrast, the medium-lived TCs were generated in the region ranging from 130°E to 150°E (i.e., the middle of the WNP region). Furthermore, we examined the MGLs of the short-, medium-, and long-lived TCs over the WNP. Compared with the MGL of all TCs over the whole WNP basin), there is no obvious difference in the

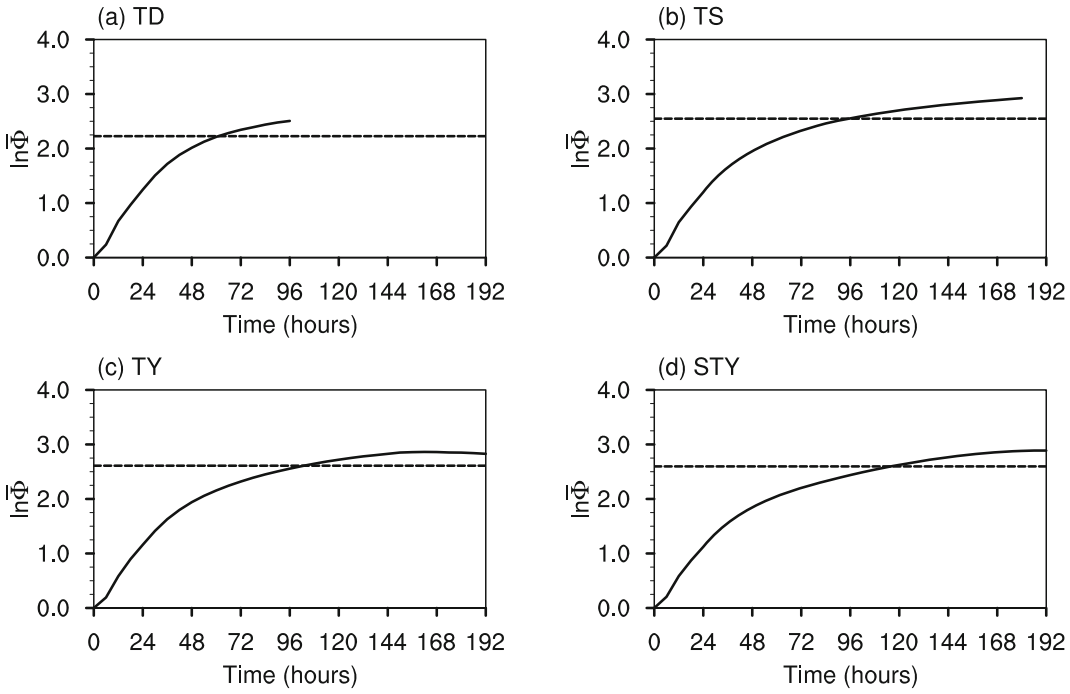

Fig. 8. As in Fig. 2 but for the mean error growth of the (a) TD, (b) TS, (c) TY, and (d) STY intensity tracks.

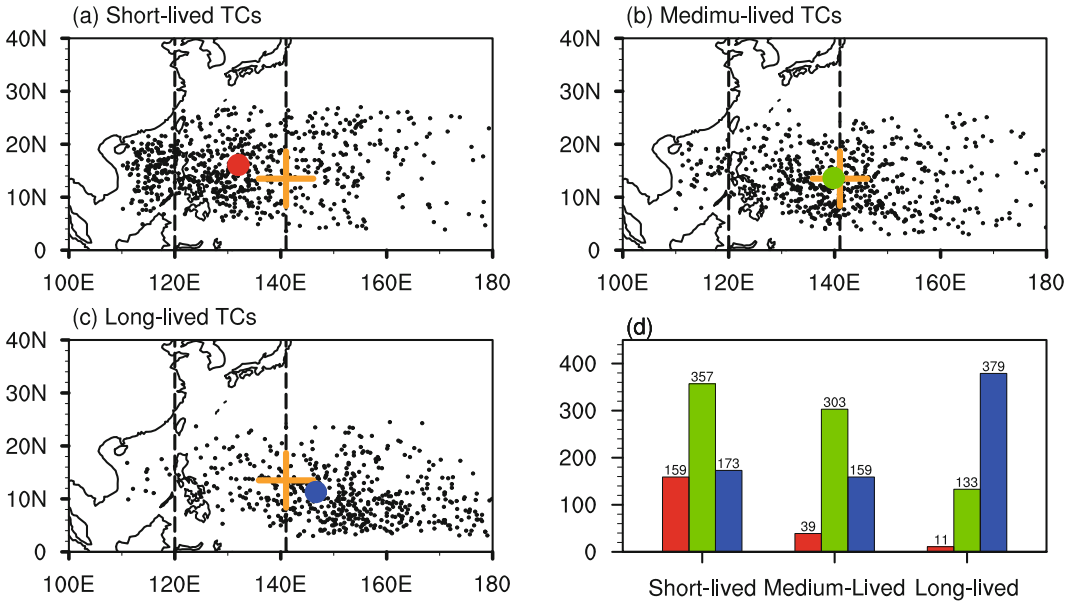

Fig. 9. Spatial distributions of the genesis locations of (a) short-lived, (b) medium-lived, and (c) long-lived TCs over the whole WNP basin. The small black dots indicate the genesis locations of the TCs and the big dots indicate the MGL of each category of TC. Crosses indicate the MGL. (d) Number of TCs generated in the three subregions for the three lifespan groups.

latitude of the MGLs of the short-, medium-, and long-lived TCs, but the longitude of the MGL differs considerably for the three groups of TCs. The MGL of the short-lived TCs is west of the MGL of all TCs, whereas the MGL of the long-lived TCs is east of the of all TCs. The longitude of the MGL also differs significantly, by 17.2°, between the short-lived and long-lived TCs. However, in contrast to the MGL of all TCs, the MGL of the medium-lived TCs is shifted slightly westwards, by about 0.4° of longitude.

The numbers of short-, medium-, and long-lived TCs generated in the SCS, WWNP, and EWNP subregions are shown in Fig. 9d. A greater number of short-lived TCs formed in the SCS and WWNP (516), i.e., nearly three times the number in the EWNP (173). In contrast, most of the long-lived TCs were generated in the EWNP (379), whereas fewer long-lived TCs were generated in the SCS and WWNP (144). These re-

sults indicate that the TC genesis location is a significant control on TC lifespan, and that the longer-lived TCs tend to be generated in the east of the WNP region, which is consistent with the findings of Chan (2005) and Wang and Chan (2002).

We also explored the relationship between TC intensity and genesis location. Figures 10a–d show the spatial distribution of TC genesis location for the four categories of TC intensity (TD, TS, TY, and STY) over the whole WNP basin. We see that more TDs and TSs were generated in the SCS and WWNP, and their MGLs are west of the MGL. The MGL of the TY group is located close to the MGL. In contrast, the MGL of the STY group is located well to the east of the MGL, and the longitude of the MGL of the STY group and the MGL differs by 6.6°. In addition, we note that the stronger TCs tend to be generated in the east of the WNP region, whereas fewer strong TCs are generated in the SCS (Fig. 10e). This result is consistent with Chan (2005), who found that the SCS does not favor the generation of strong TCs, possibly because the TCs are already close to land and tend to have a shorter lifetime.

According to the above analysis, there are close relationships among TC genesis location, lifetime, and intensity over the whole WNP basin. Stronger and longer-lived TCs tend to be generated in the east of the WNP, whereas the weaker and shorter-lived TCs tend to be generated in the west of the WNP and in the SCS. However, the question remains as to why long-lived and strong TCs generated in the EWNP tend to have a higher TC track predictability limit. To address this question, we calculated the mean tracks of all of the lifetime and intensity categories of TC (Fig. 11). For each category of TCs, its mean track is successive mean positions (including the mean longitude and latitude) of TCs at each time. The TCs in the three lifetime categories (short-, medium-, and long-lived TCs) maintain a northwestward path in the early stages, and then curve back towards the northeast. The long-lived TCs generated in the EWNP follow a northwestward track within the first 168 h (7 days), after which they curve from a northwestward to a northeastward track. In contrast, those short-lived TCs that are generated in the WWNP move northwestwards over the first 66 h (2.75 days) before changing direction. As pointed out by Leslie et al. (1998), the TCs that tend to curve track suddenly and exhibit significant erratic motion are inherently unpredictable. Wang and Chan (2002) and Wu et al. (2012) pointed out that the tracks of TCs generated in the east of the WNP tend to be steadier, and thus more predictable, before entering midlatitude waters or encountering land. We see that the four TC intensity categories also follow a northwestward track in the early stages.

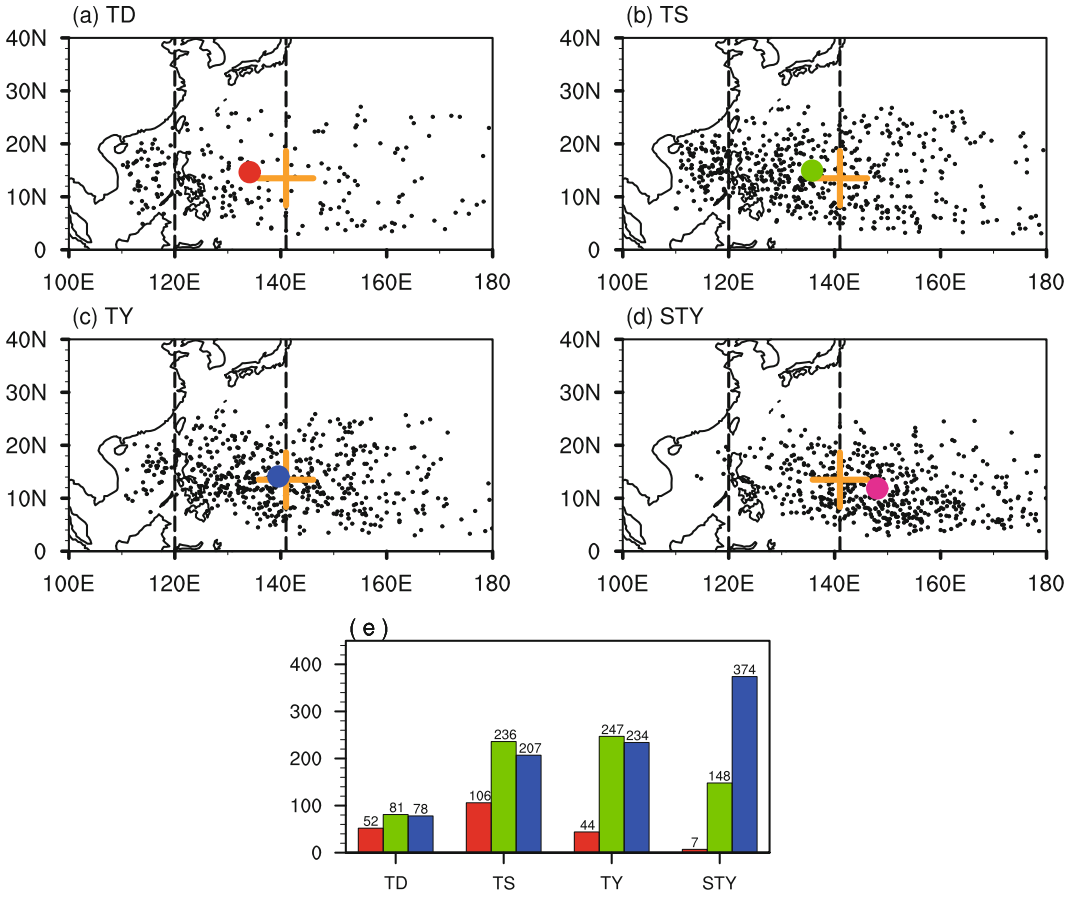

Fig. 10. As in Fig. 9 but for the spatial distributions of the genesis location of the (a) TD, (b) TS, (c) TY, and (d) STY intensity groups over the whole WNP basin. (e) Number of TCs generated in the three subregions for the four intensity categories.

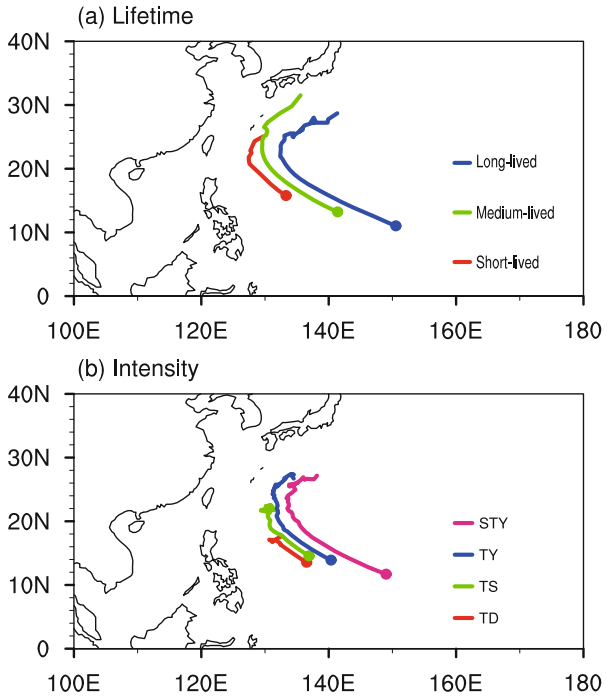

Fig. 11. Mean track of all TCs for different (a) lifetimes and (b) intensities.

However, it takes longer for the STY group (ca. 5 days) to curve northeastwards than for the TD group (ca. 2.5 days). These results indicate that the predictability of the TC tracks is closely linked to their lifetime, intensity, and genesis location. Generally speaking, the longer-lived and stronger TCs tend to be generated in the east of the WNP region, where the TCs have a relatively long travel time before they curve northeastwards, and thus tend to be more predictable. These results further suggest that TC genesis location has a significant influence on the predictability limit of TC tracks in the WNP and SCS.

5.2. *Dependence of the predictability limit on the real-time location*

Our results indicate that the predictability limit for TC tracks across the whole WNP basin is closely linked to the genesis location. In addition to the genesis location, the change in track predictability throughout the TC lifecycle is worthy of investigation. Therefore, we further examined the mean error growth of a TC track as a function of the time since the TC formed. Note that the analogous TCs are based on the similarity of the TC's real-time location at 24, 48, 72, and 96 h after TC genesis. If the reference TC was unable to find its analog TC at these four real-times, we excluded the reference TC. Figure 12 shows the mean error growth of a TC track obtained from the different real-time locations that include the genesis location (00 h), 24 h real-time location (24 h after TC genesis), 48 h real-time location (48 h after TC genesis), and 72 h real-time location (72 h after TC genesis), respectively. There are some differences in the mean error growth of the track for the TC at the different real-time

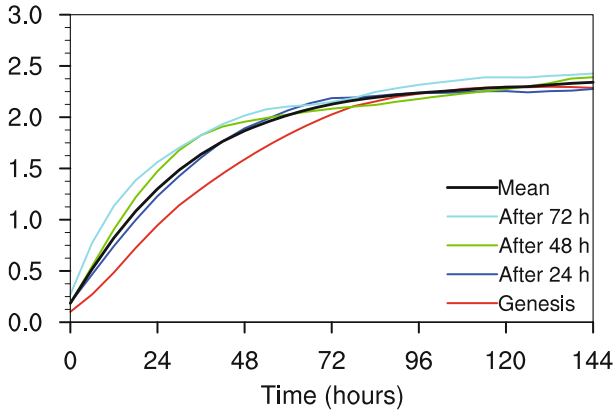

Fig. 12. Mean error growth of a TC track obtained from different real-time locations over the whole WNP basin, including the genesis location (00 h) and its real-time locations at 24, 48 and 72 h after TC genesis. The genesis time and location are defined as the time and location of the first record of a TC track, respectively.

locations. The mean error growth of tracks shows the slowest growth and takes the longest time to reach saturation state when the TC forms in the open Pacific (at genesis time, 00 h), whereas the time at which the mean error reaches saturation level is reduced for a TC at the 24, 48, and 72 h real-time locations. As reported by Leslie et al. (1998), a TC tends to have a relatively small track error or a slower error growth rate when the TC generates over the open ocean (far from continental land or islands). These results indicate that the predictability limit of a TC track gradually decreases between the genesis location and the 72 h real-time location.

6. Summary

In this study, we used the NLLE approach to estimate the predictability limit of TC tracks over the whole WNP basin using observed TC best-track data. We found that the average predictability limit of all TC tracks across the entire WNP basin was approximately 102 h (4.25 days). However, the predictability limit of the TC tracks varied widely with the genesis location, lifetime, and intensity of the TCs. The predictability limits were highest in the EWNP, followed by the WWNP, and then the SCS, with values of about 108 h (4.5 days), 84 h (3.5 days), and 60 h (2.5 days), respectively. Moreover, the predictability limit of the TC tracks tended to increase with increasing TC lifetime, and the predictability limits of the TC tracks for short-, medium-, and long-lived TCs were approximately 72 h (3 days), 120 h (5 days), and 132 h (5.5 days), respectively. Likewise, the predictability limits of the TC tracks also differed with TC intensity, and the predictability limits of the TC tracks for the TD, TS, TY, and STY intensity categories were about 60 h (2.5 days), 96 h (4 days), 102 h (4.25 days), and 114 h (4.75 days), respectively.

Further analysis indicated that the predictability limit of the TC tracks, and the lifetime, intensity, and genesis location

of the TCs, are closely related. We found that the relatively strong and long-lived TCs tend to be generated in the EWNP, whereas the relatively weak and short-lived TCs tend to form in the WWNP and SCS. As the relatively strong and long-lived (weak and short-lived) TCs generated in the EWNP (WWNP and SCS) have a relatively long (short) travel time before they curve northeastwards, they tend to have a high (low) predictability limit. The link among the predictability limit of the TC tracks, lifetime, intensity, and genesis location of the TCs highlights the potential importance of the genesis location in contributing to TC predictability.

In this paper, the predictability limit of TC tracks over the whole WNP basin was quantitatively estimated using observed TC track data. Given the relatively short observational records of observed TC track data, our estimation of the predictability limit of the TC tracks will inevitably include large uncertainties. Further study is required to assess the predictability of TC tracks using the best-track data from a longer period of observation or a long-term simulation by a more realistic TC model. In addition, to gain a more complete understanding of TCs, it will be necessary to investigate the predictability of TC intensity in our future work.

Acknowledgements. This research was jointly supported by the National Natural Science Foundation of China for Excellent Young Scholars (Grant No. 41522502), the National Program on Global Change and Air–Sea Interaction (Grant No. GASI-IPOVAI-03, GASI-IPOVAI-06), the Beijige Open Research Fund for Nanjing Joint Center of Atmospheric Research (Grant No. NJCAR2018ZD03), and the National Key Technology Research and Development Program of the Ministry of Science and Technology of China (Grant No. 2015BAC03B07).

APPENDIX A

Algorithm for finding two analogous TCs

Let the TC $\{x_i(\theta_i(t_k),\varphi_i(t_k)), k = 0,1,2,\cdots\cdots,M-1, i = 1,2,\cdots\cdots,N\}$ be a set of points indicating TC position, where M represents the length of a TC time series, N represents the total number of TCs, and $\theta_i(t_k)$ and $\varphi_i(t_k)$ represent the longitude and latitude, respectively. For a continuous series of points describing the evolving TC position, the distance (along a great circle) between two independent TCs is given by

$$d_{i,j}(t_k) = R\arccos\{\sin\varphi_i(t_k)\sin\varphi_j(t_k) + \cos\varphi_i(t_k)\cos\varphi_j(t_i)[\theta_i(t_k)-\theta_j(t_k)]\}\,, \quad \text{(A1)}$$

where i and j are the serial number of TC, k is the serial number of time, R is the average radius of the Earth and t_k are the times of TC_i and TC_j.

The determinations of two analogous TCs are based on the initial distance $d_{i,j}(t_0)$ and the evolutionary distance d_e. A brief description of the algorithm that we used to find two analogous TCs from all TCs over the WNP basin is given below:

Step 1. Taking the genesis location $x_1(\theta_1(t_0),\varphi_1(t_0))$ of TC_1 as a reference initial position at the initial time (genesis time) t_0, we first seek the genesis location $x_j(\theta_j(t_0),\varphi_j(t_0))$ of TC_j. The initial distance $d_{1,j}(t_0)$ is the distance between the genesis locations of TC_1 and TC_j. To ensure the similarity of the large-scale environmental steering flows for the two TCs, the reference TC (TC_1) and TC_j should have formed in a similar "season" in different years (i.e., ±45 days of the genesis time of the reference TC), and the difference in initial intensity between TC_1 and TC_j should be less than 10 kt.

Step 2. Within a short initial period, the evolutionary distance d_e is used to measure the degree of similarity of the motion direction between TC_1 and TC_j. Note that in a previous study, the choice of the initial evolutionary stage depended on the persistence of the variable of interest (Li and Ding, 2011). In the present study, because it is impossible to obtain the persistence of the TC tracks, we set the initial evolution stage as two 6-h time steps (i.e., 12 h), and we find that the predictability results of the TC tracks obtained are not sensitive to the choice of this parameter. During the initial evolutionary stage, the evolutionary distance d_e between TC_1 $x_1(\theta_1(t_k),\varphi_1(t_k))$ and TC_j $x_j(\theta_j(t_k),\varphi_j(t_k))$ is given by

$$d_\mathrm{e} = \sqrt{\frac{1}{K+1}\sum_{k=0}^{K}[d_{1,j}(t_k)]^2}, \quad K = 2,3,4 \quad \text{(A2)}$$

where K is the steps of the evolutionary interval and $d_{1,j}(t_k)$ is the amount of distance between TC_1 $x_1(\theta_1(t_k),\varphi_1(t_k))$ and TC_j $x_j(\theta_j(t_k),\varphi_j(t_k))$.

Step 3. The total distance d_t, considering not only the initial distance within range of 50 km between two independent TCs, but also the evolutionary distance, which should be less than 100 km during their evolution, is found by adding $d_{1,j}(t_0)$ and d_e:

$$d_\mathrm{t} = d_{1,j}(t_0) + d_\mathrm{e}\,. \quad \text{(A3)}$$

If the total distance d_t is very small, it is likely that TC_1 $x_1(\theta_1(t_k),\varphi_1(t_k))$ and TC_j $x_j(\theta_j(t_k),\varphi_j(t_k))$ have a similar genesis location and movement direction. The constraint of the total distance d_t, which contains both initial information and evolutionary information over an initial evolutionary period, allows us to exclude a large portion of all the non-analogous TCs, thereby helping us to find a true analogous TC_j for the reference TC_1.

APPENDIX B

Algorithm for NLLE and RGIE estimation from best-track data

For every TC_i $\{x_i(\theta_i(t_k),\varphi_i(t_k)), k = 0,1,2,3,\cdots\cdots,M-1\}$, the total distance d_t can be determined based on the algorithm in Appendix A. The TC_j $\{x_j(\theta_j(t_k),\varphi_j(t_k)), k = 0,1,2,\cdots\cdots,M-1\}$ that is analogous to the reference TC_i can be chosen from all TCs over the whole WNP basin if the total distance d_t is very small. The procedure of the estimate of NLLE and RGIE is outlined below:

Step 1. The initial distance is the distance between the genesis locations (along a great circle) of the reference TC$_i$ and its analogous TC$_j$, as follows:

$$L_i(t_0) = R\arccos\{\sin\varphi_i(t_0)\sin\varphi_j(t_0) + \cos\varphi_i(t_0)\cos\varphi_j(t_0)[\theta_i(t_0)-\theta_j(t_0)]\}\,. \quad \text{(B1)}$$

Step 2. At time $t_k = k\times\Delta$ $(k = 1,2,\cdots,M)$, the reference TC$_i$ will have moved from $x_i(\theta_i(t_0),\varphi_i(t_0))$ to $x_i(\theta_i(t_k),\varphi_i(t_k))$, and the analogous TC$_j$ will have moved from $x_j(\theta_j(t_0),\varphi_j(t_0))$ to $x_j(\theta_j(t_k),\varphi_j(t_k))$ (see Fig. 1b). The initial difference $L_i(t_0)$ will have become

$$L_i(t_k) = R\arccos\{\sin\varphi_i(t_k)\sin\varphi_j(t_k) + \cos\varphi_i(t_k)\cos\varphi_j(t_k)[\theta_i(t_k)-\theta_j(t_k)]\}\,. \quad \text{(B2)}$$

To estimate the NLLE, it is necessary to examine the growth rate of the distance between two initially close TCs over the whole WNP basin. The growth rate of the initial error (initial distance) during the evolutionary interval (t_k) is

$$\xi_i(t_k) = \frac{1}{t_k}\ln\frac{L_i(t_k)}{L_i(t_0)},\ (k = 1,2,3,\cdots\cdots,M)\,, \quad \text{(B3)}$$

where $L_i(t_0)$ is the initial distance between the reference TC$_i$ $x_i(\theta_i(t_k),\varphi_i(t_k))$ and its analogous TC$_j$, and $L_i(t_k)$ is the evolution of $L_i(t_0)$ with time t_k. With k gradually increasing, we can obtain the variation in $\xi_i(t_k)$ as a function of evolved time t_k $(k = 1,2,3,\cdots\cdots,M)$.

Step 3. The above procedure is repeated for each TC, and we obtain the error growth rate for all reference TC locations $\{[x_1(t_k),x_2(t_k),\cdots\cdots,x_i(t_k)],(i = 1,2,3,\cdots\cdots,N)\}$ as follows:

$$\xi_i(t_k) = \frac{1}{t_k}\ln\frac{L_i(t_k)}{L_i(t_0)},\ (i=1,2,3\cdots\cdots,N;k=1,2,3,\cdots\cdots,M)\,, \quad \text{(B4)}$$

where $i = N$ is the total number of TCs over the whole WNP basin, $t_k = k\times\Delta$ $(k = 1,2,3,\cdots\cdots,M)$ is the evolution time, $L_i(t_0)$ is the initial distance between the reference TC $x_i(\theta_i(t_0),\varphi_i(t_0))$ and its analogous TC, and $L_i(t_k)$ is the evolution of $L_i(t_0)$ at time t_k. It follows that the average of the error growth rates for all reference TCs is

$$\bar{\xi}(t_k) = \frac{1}{N}\sum_{i=1}^{N}\xi_i(t_k) = \frac{1}{N}\sum_{i=1}^{N}\left[\frac{1}{t_k}\ln\frac{L_i(t_k)}{L_i(t_0)}\right] = \frac{1}{t_k}\ln\left[\sqrt[N]{\frac{L_1(t_k)}{L_1(t_0)}\frac{L_2(t_k)}{L_2(t_0)}\cdots\cdots\frac{L_N(t_k)}{L_N(t_0)}}\right]. \quad \text{(B5)}$$

That is,

$$\exp[\bar{\xi}(t_k)t_k] = \sqrt[N]{\frac{L_1(t_k)}{L_1(t_0)}\frac{L_2(t_k)}{L_2(t_0)}\cdots\cdots\frac{L_N(t_k)}{L_N(t_0)}}\,. \quad \text{(B6)}$$

Step 4. Observing that the right-hand-side of Eq. (B6) is the geometric mean of the relative growth of initial error (i.e., RGIE) of all reference TCs, we obtain the approximation of the mean RGIE as follows:

$$\bar{\Phi}(t_k) = \exp[\bar{\xi}(t_k)t_k],\ (k = 1,2,3,\cdots\cdots,M)\,. \quad \text{(B7)}$$

By investigating the evolution of $\bar{\Phi}(t_k)$ with increasing t_k, the time at which the mean error reaches 95% of the saturation level can be defined as the mean predictability limit for all TC tracks.

REFERENCES

Aberson, S. D., 1998: Five-day tropical cyclone track forecasts in the North Atlantic basin. *Wea. Forecasting*, **13**, 1005–1015, https://doi.org/10.1175/1520-0434(1998)013<1005:FDTCTF>2.0.CO;2.

Aberson, S. D., and C. R. Sampson, 2003: On the predictability of tropical cyclone tracks in the Northwest Pacific basin. *Mon. Wea. Rev.*, **131**, 1491–1497, https://doi.org/10.1175/1520-0493(2003)131<1491:OTPOTC>2.0.CO;2.

Aiyyer, A., 2015: Recurving western North Pacific tropical cyclones and midlatitude predictability. *Geophys. Res. Lett.*, **42**, 7799–7807, https://doi.org/10.1002/2015GL065082.

Arpe, K., and E. Klinker, 1986: Systematic errors of the ECMWF operational forecasting model in mid-latitudes. *Quart. J. Roy. Meteor. Soc.*, **112**, 181–202, https://doi.org/10.1002/qj.49711247111.

Bender, M. A., R. J. Ross, R. E. Tuleya, and Y. Kurihara, 1993: Improvements in tropical cyclone track and intensity forecasts using the GFDL initialization system. *Mon. Wea. Rev.*, **121**, 2046–2061, https://doi.org/10.1175/1520-0493(1993)121<2046:IITCTA>2.0.CO;2.

Camargo, S. J., and A. H. Sobel, 2005: Western North Pacific tropical cyclone intensity and ENSO. *J. Climate*, **18**, 2996–3006, https://doi.org/10.1175/JCLI3457.1.

Camargo, S. J., K. A. Emanuel, and A. H. Sobel, 2007: Use of a genesis potential index to diagnose ENSO effects on tropical cyclone genesis. *J. Climate*, **20**, 4819–4834, https://doi.org/10.1175/JCLI4282.1.

Chan, J. C. L., 2005: Interannual and interdecadal variations of tropical cyclone activity over the western North Pacific. *Meteor. Atmos. Phys.*, **89**, 143–152, https://doi.org/10.1007/s00703-005-0126-y.

Chan, J. C. L., and W. M. Gray, 1982: Tropical cyclone movement and surrounding flow relationships. *Mon. Wea. Rev.*, **110**, 1354–1374, https://doi.org/10.1175/1520-0493(1982)110<1354:TCMASF>2.0.CO;2.

Chen, B. H., J. P. Li, and R. Q. Ding, 2006: Nonlinear local Lyapunov exponent and atmospheric predictability research. *Science in China Series D*: *Earth Sciences*, **49**, 1111–1120, https://doi.org/10.1007/s11430-006-1111-0.

Dalcher, A., and E. Kalnay, 1987: Error growth and predictability in operational ECMWF forecasts. *Tellus A*, **39**, 474–491, https://doi.org/10.3402/tellusa.v39i5.11774.

Ding, R. Q., and J. P. Li, 2007: Nonlinear finite-time Lyapunov exponent and predictability. *Physics Letters A*, **364**, 396–400, https://doi.org/10.1016/j.physleta.2006.11.094.

Ding, R. Q., and J. P. Li, 2009a: Decadal and seasonal dependence of North Pacific sea surface temperature persistence. *J. Geophys. Res.*, **114**, https://doi.org/ 10.1029/2008JD010723.

Ding, R. Q., and J. P. Li, 2009b: Long-Term trend and decadal variability of persistence of daily 500-mb geopotential height

anomalies during boreal winter. *Mon. Wea. Rev*., **137**, 3519–3534, https://doi.org/10.1175/2009MWR2841.1.

Ding, R. Q., and J. P. Li, 2012: Relationships between the limit of predictability and initial error in the uncoupled and coupled lorenz models. *Adv. Atmos. Sci*., **29**, 1078–1088, https://doi.org/10.1007/s00376-012-1207-8.

Ding, R. Q., G. L. Feng, S. D. Liu, S. K. Liu, S. X. Huang, and Z. T. Fu, 2007: Nonlinear atmospheric and climate dynamics in China (2003–2006): A review. *Adv. Atmos. Sci*., **24**, 1077–1085, https://doi.org/10.1007/s00376-007-1077-7.

Ding, R. Q., J. P. Li, and K. H. Seo, 2010: Predictability of the madden-julian oscillation estimated using observational data. *Mon. Wea. Rev*., **138**, 1004–1013, https://doi.org/10.1175/2009MWR3082.1.

Ding, R. Q., J. P. Li, F. Zheng, J. Feng, and D. Q. Liu, 2016: Estimating the limit of decadal-scale climate predictability using observational data. *Climate Dyn*., **46**, 1563–1580, https://doi.org/10.1007/s00382-015-2662-6.

Elsberry, R. L., 2007: Advances in tropical cyclone motion prediction and recommendations for the future. *WMO Bull*., **56**, 131–134.

Elsberry, R. L., 2014: Advances in research and forecasting of tropical cyclones from 1963–2013. *Asia-Pacific Journal of Atmospheric Sciences*, **50**, 3–16, https://doi.org/10.1007/s13143-014-0001-1.

Elsberry, R. L., and J. E. Peak, 1986: An evaluation of tropical cyclone forecast aids based on cross-track and along-track components. *Mon. Wea. Rev.*, **114**, 147–155, https://doi.org/10.1175/1520-0493(1986)114<0147:AEOTCF>2.0.CO;2.

Elsberry, R. L., M. S. Jordan, and F. Vitart, 2010: Predictability of tropical cyclone events on intraseasonal timescales with the ECMWF monthly forecast model. *Asia-Pacific Journal of Atmospheric Sciences*, **46**, 135–153, https://doi.org/10.1007/s13143-010-0013-4.

Fiorino, M., 2009: Record-setting performance of the ECMWF IFS in medium-range tropical cyclone track prediction. *ECMWF Newsletter*, **118**, 20–27.

Fraedrich, K., 1987: Estimating weather and climate predictability on attractors. *J. Atmos. Sci*., **44**, 722–728, https://doi.org/10.1175/1520-0469(1987)044<0722:EWACPO>2.0.CO;2.

Fraedrich, K., and L. M. Leslie, 1989: Estimates of cyclone track predictability. I: Tropical cyclones in the Australian region. *Quart. J. Roy. Meteor. Soc*., **115**, 79–92, https://doi.org/10.1002/qj.49711548505.

Goerss, J. S., 2000: Tropical cyclone track forecasts using an ensemble of dynamical models. *Mon. Wea. Rev*., **128**, 1187–1193, https://doi.org/10.1175/1520-0493(2000)128<1187:Tctfua>2.0.Co;2.

Goerss, J. S., 2009: Impact of satellite observations on the tropical cyclone track forecasts of the navy operational global atmospheric prediction system. *Mon. Wea. Rev*., **137**, 41–50, https://doi.org/10.1175/2008MWR2601.1.

Grassberger, P., and I. Procaccia, 1984: Dimensions and entropies of strange attractors from a fluctuating dynamics approach. *Physica D*: *Nonlinear Phenomena*, **13**, 34–54, https://doi.org/10.1016/0167-2789(84)90269-0.

Heckley, W. A., 1985: Systematic errors of the ECMWF operational forecasting model in tropical regions. *Quart. J. Roy. Meteor. Soc*., **111**, 709–738, https://doi.org/10.1002/qj.49711146904.

Kazantsev, E., 1999: Local Lyapunov exponents of the quasi-geostrophic ocean dynamics. *Applied Mathematics and Computation*, **104**, 217–257, https://doi.org/10.1016/S0096-3003(98)10078-4.

Knapp, K. R., M. C. Kruk, D. H. Levinson, H. J. Diamond, and C. J. Neumann, 2010: The international best track archive for climate stewardship (IBTrACS): unifying tropical cyclone data. *Bull. Amer. Meteor. Soc*., **91**, 363–376, https://doi.org/10.1175/2009BAMS2755.1.

Knutson, T. R., and Coauthors, 2010: Tropical cyclones and climate change. *Nature Geoscience*, **3**, 157–163, https://doi.org/10.1038/ngeo779.

Lacarra, J. F., and O. Talagrand, 1988: Short-range evolution of small perturbations in a barotropic model. *Tellus A*, **40**, 81–95, https://doi.org/10.1111/j.1600-0870.1988.tb00408.x.

Leslie, L. M., R. F. Abbey Jr., and G. J. Holland, 1998: Tropical cyclone track predictability. *Meteor. Atmos. Phys*., **65**, 223–231, https://doi.org/10.1007/BF01030790.

Li, J. P., and R. Q. Ding, 2011: Temporal-spatial distribution of atmospheric predictability limit by local dynamical analogs. *Mon. Wea. Rev*., **139**, 3265–3283, https://doi.org/10.1175/Mwr-D-10-05020.1.

Li, J. P., and R. Q. Ding, 2013: Temporal-spatial distribution of the predictability limit of monthly sea surface temperature in the global oceans. *Int. J. Climatol.*, **33**, 1936–1947, https://doi.org/10.1002/joc.3562.

Li, W. J., J. P. Liu, L. J. Chen, P. Q. Zhang, and H. L. Ren, 2014: Spatiotemporal distribution and decadal change of the monthly temperature predictability limit in China. *Chinese Science Bulletin*, **59**, 4864–4872, https://doi.org/10.1007/s11434-014-0502-4.

Li, W. W., Z. Wang, and M. S. Peng, 2016: Evaluating tropical cyclone forecasts from the NCEP global ensemble forecasting system (GEFS) reforecast version 2. *Wea. Forecasting*, **31**, 895–916, https://doi.org/10.1175/WAF-D-15-0176.1.

Liu, J. P., W. J. Li, L. J. Chen, J. Q. Zuo, and P. Q. Zhang, 2016: Estimation of the monthly precipitation predictability limit in China using the nonlinear local lyapunov exponent. *Journal of Meteorological Research*, **30**, 93–102, https://doi.org/10.1007/s13351-015-5049-z.

Lorenz, E. N., 1963: Deterministic nonperiodic flow. *J. Atmos. Sci*., **20**, 130–141, https://doi.org/10.1175/1520-0469(1963)020<0130:Dnf>2.0.Co;2.

Lorenz, E. N., 1969: Atmospheric predictability as revealed by naturally occurring analogues. *J. Atmos. Sci*., **26**, 636–646, https://doi.org/10.1175/1520-0469(1969)26<636:Aparbn>2.0.Co;2.

Mu, M., 2000: Nonlinear singular vectors and nonlinear singular values. *Science in China Series D*: *Earth Sciences*, **43**, 375–385, https://doi.org/10.1007/BF02959448.

Munsell, E. B., 2016: Dynamics and predictability of tropical cyclones evaluated through convection-permitting ensemble analyses and forecasts with airborne radar and sounding observations. PhD dissertation, The Pennsylvania State University.

Munsell, E. B., and F. Q. Zhang, 2014: Prediction and uncertainty of Hurricane Sandy (2012) explored through a real-time cloud-permitting ensemble analysis and forecast system assimilating airborne Doppler radar observations. *Journal of Advances in Modeling Earth Systems*, **6**, 38–58, https://doi.org/10.1002/2013MS000297.

Murakami, H., B. Wang, and A. Kitoh, 2011: Future change of western North Pacific typhoons: projections by a 20-km-mesh global atmospheric model. *J. Climate*, **24**, 1154–1169,

https://doi.org/10.1175/2010JCLI3723.1.

Nicolis, C., and G. Nicolis, 1984: Is there a climatic attractor? *Nature*, **311**, 529–532, https://doi.org/10.1038/311529a0.

Peng, S. Q., and Coauthors, 2015: A Real-time regional forecasting system established for the South China Sea and its performance in the track forecasts of tropical cyclones during 2011-13. *Wea. Forecasting*, **30**, 471–485, https://doi.org/10.1175/Waf-D-14-00070.1.

Plu, M., 2011: A New Assessment of the predictability of tropical cyclone tracks. *Mon. Wea. Rev*., **139**, 3600–3608, https://doi.org/10.1175/2011MWR3627.1.

Poterjoy, J., and F. Q. Zhang, 2014: Predictability and genesis of hurricane karl (2010) examined through the EnKF assimilation of field observations collected during PREDICT. *J. Atmos. Sci.*, **71**, 1260–1275, https://doi.org/10.1175/JAS-D-13-0291.1.

Qi, L. B., H. Yu, and P. Y. Chen, 2014: Selective ensemble-mean technique for tropical cyclone track forecast by using ensemble prediction systems. *Quart. J. Roy. Meteor. Soc*., **140**, 805–813, https://doi.org/10.1002/qj.2196.

Qin, X. H., W. S. Duan, and M. Mu, 2013: Conditions under which CNOP sensitivity is valid for tropical cyclone adaptive observations. *Quart. J. Roy. Meteor. Soc*., **139**, 1544–1554, https://doi.org/10.1002/qj.2109.

Sampson, C. R., J. S. Goerss, and H. C. Weber, 2006: Operational performance of a new barotropic model (WBAR) in the western North Pacific basin. *Wea. Forecasting*, **21**, 656–662, https://doi.org/10.1175/WAF939.1.

Shi, Z., and R. Q. Ding, 2012: Estimating the predictability of the Quasi-Biweekly Oscillation using the nonlinear local Lyapunov exponent approach. *Atmospheric and Oceanic Science Letters*, **5**, 389–392, https://doi.org/10.1080/16742834.2012.11447023.

Thanh, C., T. T. Tien, and K. Q. Chanh, 2016: Application of breeding ensemble to tropical cyclone track forecasts using the Regional Atmospheric Modeling System (RAMS) model. *Applied Mathematical Modelling*, **40**, 8309–8325, https://doi.org/10.1016/j.apm.2016.04.010.

Thompson, P. D., 1957: Uncertainty of initial state as a factor in the predictability of large scale atmospheric flow patterns. *Tellus*, **9**, 275–295, https://doi.org/10.1111/j.2153-3490.1957.tb01885.x.

Walsh, K. J., and Coauthors, 2016: Tropical cyclones and climate change. *Wiley Interdisciplinary Reviews*: *Climate Change*, **7**, 65–89, https://doi.org/10.1002/wcc.371.

Wang, B., and J. C. L. Chan, 2002: How strong ENSO events affect tropical storm activity over the western North Pacific. *J. Climate*, **15**, 1643–1658, https://doi.org/10.1175/1520-0442(2002)015<1643:HSEEAT>2.0.CO;2.

Wang, G. H., J. L. Su, Y. H. Ding, and D. K. Chen, 2007: Tropical cyclone genesis over the South China Sea. *J. Mar. Syst*., **68**, 318–326, https://doi.org/10.1016/j.jmarsys.2006.12.002.

Wong, M. L. M., and J. C. L. Chan, 2006: Tropical cyclone motion in response to land surface friction. *J. Atmos. Sci*., **63**, 1324–1337, https://doi.org/10.1175/JAS3683.1.

Wu, L., Z. P. Wen, R. H. Huang, and R. G. Wu, 2012: Possible linkage between the monsoon trough variability and the tropical cyclone activity over the western North Pacific. *Mon. Wea. Rev*., **140**, 140–150, https://doi.org/10.1175/MWR-D-11-00078.1.

Yan, Y. F., Y. Q. Qi, and W. Zhou, 2012: Variability of tropical cyclone occurrence date in the South China Sea and its relationship with SST warming. *Dyn. Atmos. Oceans*, **55–56**, 45–59, https://doi.org/10.1016/j.dynatmoce.2012.05.001.

Yoden, S., and M. Nomura, 1993: Finite-time Lyapunov stability analysis and its application to atmospheric predictability. *J. Atmos. Sci*., **50**, 1531–1543, https://doi.org/10.1175/1520-0469(1993)050<1531:FTLSAA>2.0.CO;2.

Zhang, W. J., Y. J. Zhang, D. Zheng, and X. J. Zhou, 2012: Lightning distribution and eyewall outbreaks in tropical cyclones during landfall. *Mon. Wea. Rev*., **140**, 3573–3586, https://doi.org/10.1175/MWR-D-11-00347.1.

Zhang, Z., and T. N. Krishnamurti, 1997: Ensemble forecasting of hurricane tracks. *Bull. Amer. Meteor. Soc*., **78**, 2785–2796, https://doi.org/10.1175/1520-0477(1997)078<2785:Efoht>2.0.Co;2.

Ziehmann, C., L. A. Smith, and J. Kurths, 2000: Localized Lyapunov exponents and the prediction of predictability. *Physics Letters A*, **271**, 237–251, https://doi.org/10.1016/S0375-9601(00)00336-4.